

# Tunable Massive Dirac Fermions in Ferromagnetic $\text{Fe}_3\text{Sn}_2$ Kagome Lattice

Zheng-Zhe Lin\* and Xi Chen

**Kagome lattice is known to host Dirac electrons with exotic quantum magnetic states, which can lead to topological and Chern insulating phases. A recent experiment has found that  $\text{Fe}_3\text{Sn}_2$  kagome lattice supports massive Dirac fermions in the presence of ferromagnetic order. Herein, the origin of the effective mass of Dirac electrons in  $\text{Fe}_3\text{Sn}_2$  is theoretically interpreted. By investigating the formation mechanism of spin-polarized Dirac states, the relation of spin-orbit coupling (SOC) and effective mass are clarified. On this basis, a method to control the effective mass of Dirac electrons is proposed. The results reveal the origin of new phenomenon in spin-polarized Dirac quantum systems with time-reversal symmetry breaking. The study on the modulation of Dirac electrons provides insight into a modulation mechanism based on SOC and guidance to the miniaturization of high-mobility electronic and spintronic devices.**

Topological materials are a new class of quantum matters including topological insulators,<sup>[1,2]</sup> topological crystal insulators,<sup>[3]</sup> Dirac semimetals,<sup>[4,5]</sup> Weyl semimetals,<sup>[6–8]</sup> nodal-line semimetals,<sup>[9–12]</sup> and so on. In the past decade, topological materials have received great attention due to their novel physical properties and behaviors. Recently, a scheme for quantum computing based on Majorana zero-energy mode was proposed.<sup>[13]</sup> The study of topological materials can not only bring emerging applications to the field of electronics, but also help us to understand the new states of quantum matters. The novel physical properties of Dirac semimetals,<sup>[14–20]</sup> e.g., Klein tunneling, have attracted research interests of physicists. The low-energy effective Hamiltonian near the Dirac point behaves as massless (2+1)-dimensional Dirac particles. So far, most of the research on Dirac fermions has been concerned with the nonmagnetic system with time-reversal symmetry. Dirac points of these systems are not easy to be controlled due to lack of coupling with magnetic field. Therefore, it is necessary to conduct further studies on ferromagnetic Dirac systems.

A spin-unpolarized Dirac node can be viewed as a fourfold degenerate “kissing” point. Without necessary crystalline

symmetries, the Dirac nodes on the high-symmetry points or lines in the Brillouin zone may be split into two Weyl nodes with opposite spin directions. In recent years, Weyl fermions have been found in ferromagnetic systems.<sup>[21–24]</sup> These systems with time-reversal symmetry breaking can be directly coupled with the magnetic field to achieve the modulation of the transport and spintronic properties of electrons. In contrast, the fourfold degenerate Dirac points may also be split into two nodes with different energies (Figure S1, Supporting Information). The split Dirac nodes have different spin directions with time-reversal symmetry breaking. These Dirac points are not topologically stable against the mass term, which breaks the  $\gamma^5$  symmetry and opens a bandgap.<sup>[25]</sup> Lately, massive Dirac

fermions have been found in ferromagnetic  $\text{Fe}_3\text{Sn}_2$  kagome lattice.<sup>[26]</sup> The Dirac electrons in  $\text{Fe}_3\text{Sn}_2$  have unitary spin direction. Spin-orbit coupling (SOC) opens the gap of Dirac cone and gives effective mass to the Dirac electrons. Temperature-independent intrinsic anomalous Hall conductivity was observed, which suggests a prominent Berry curvature from the time-reversal-symmetry-breaking electronic bands of the kagome plane. In layered ferromagnetic crystals, spin-polarized itinerant electrons travel freely along the layers with less resistance. The effective mass of Dirac electrons can be directly controlled by the magnetic field. The study on the modulation of transport properties of Dirac electrons will be beneficial to the miniaturization of high-mobility electronic and spintronic devices.

Dirac systems present novel quantum effects. A study on these systems is of great significance for understanding phase, symmetry, and other basic physics and is closely relative to the development of quantum information technology. In this article, the mechanism for obtaining the effective mass of (2+1)-dimensional Dirac electrons in  $\text{Fe}_3\text{Sn}_2$  is theoretically interpreted. The formation of spin-polarized Dirac states is investigated, and the relation of SOC and effective mass of Dirac electrons is clarified. This work reveals the physical origin of a new phenomenon in Dirac quantum systems and proposes mechanisms for modulating energy bands and topological properties of kagome lattices. A method to control effective mass of Dirac electrons is then proposed. The results would provide guidance for future applications of Dirac materials.

As shown in **Figure 1a**, the lattice of  $\text{Fe}_3\text{Sn}_2$  (space group  $R\bar{3}m$ ) is composed of  $\text{Fe}_3\text{Sn}$  bilayer and Sn layer, alternatively stacking along the *c*-axis perpendicular to layer planes. Each  $\text{Fe}_3\text{Sn}$  bilayer

Prof. Z.-Z. Lin, Dr. X. Chen  
Department of Applied Physics  
School of Physics and Optoelectronic Engineering  
Xidian University  
Xi'an 710071, China  
E-mail: zzlin@xidian.edu.cn

 The ORCID identification number(s) for the author(s) of this article can be found under <https://doi.org/10.1002/pssr.201900705>.

DOI: 10.1002/pssr.201900705

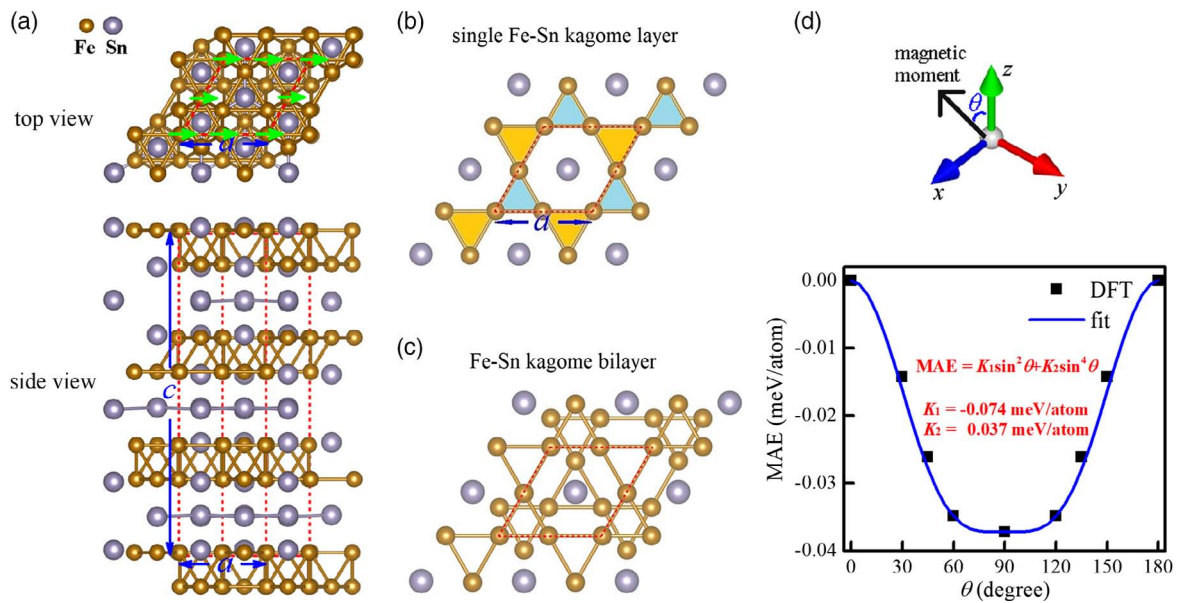


**Figure 1.** Basic properties of  $\text{Fe}_3\text{Sn}_2$ . a) The atomic structure of  $\text{Fe}_3\text{Sn}_2$  lattice. The unit cell is enclosed by the dashed lines. The green arrows denote magnetic moments of Fe atoms in the ground state. b) A single  $\text{Fe}_3\text{Sn}$  layer in  $\text{Fe}_3\text{Sn}_2$ . c)  $\text{Fe}_3\text{Sn}$  bilayer in  $\text{Fe}_3\text{Sn}_2$ . d) MAE of  $\text{Fe}_3\text{Sn}_2$  lattice varying with the angle  $\theta$  between the magnetic moment of the cell and the z-axis.

includes two Fe kagome layers with Sn atoms embedded in the centers of Fe hexagons (Figure 1b). The Fe kagome layers have two kinds of equilateral triangles (yellow and cyan ones) with different Fe–Fe bond lengths. In neighboring kagome layers, the Fe triangles with small side lengths (cyan ones) orient to opposite directions (Figure 1c). The Fe triangles with small side lengths in neighboring layers bond with each other and make up Fe octahedra. Sandwiched between  $\text{Fe}_3\text{Sn}$  kagome layers are Sn honeycomb layers. Density-functional theory (DFT) Perdew–Burke–Ernzerhof (PBE) calculation provides hexagonal lattice constants  $a = 5.328 \text{ \AA}$  and  $c = 19.782 \text{ \AA}$ , which are in agreement with previous experiments.<sup>[26,38]</sup> The lengths of Fe–Fe bonds in a kagome layer are 2.543 and 2.785  $\text{ \AA}$ . The interlayer distance of the neighboring kagome layers is 2.094  $\text{ \AA}$ .

A previous study measured a high Curie temperature of  $T_C = 670 \text{ K}$ .<sup>[39]</sup> DFT calculations reveal that all the magnetic moments are located on Fe atoms, with  $\mu = 2.05 \mu_B \text{ atom}^{-1}$  at the level of PBE, which is in agreement with the recent experiment ( $\mu = 1.9 \mu_B \text{ atom}^{-1}$ ).<sup>[26]</sup> In the ground state, all the magnetic moments of Fe atoms lie in the kagome plane and point to a same direction (Figure 1a). In contrast, the LDA functional gives  $\mu = 1.65 \mu_B \text{ atom}^{-1}$ . We also test the Hubbard  $U$  correction to the LDA functional. With the effective  $U = 2.0, 4.0,$  and  $6.0 \text{ eV}$ , the magnetic moments are overestimated to be  $\mu = 2.23, 2.52,$  and  $2.75 \mu_B \text{ atom}^{-1}$ , respectively. PBE +  $U$  even worsens the overestimation. Moreover, LDA or LDA +  $U$  with  $U = 2.0$  or  $4.0 \text{ eV}$  slightly underestimates the lattice parameters by about 1–3%. A proper larger  $U$  can give accurate lattice parameters, but it yields an overlarge magnetic moment. Overall, the previously mentioned comparison calculations suggest that the PBE functional can accurately describe the structure and magnetic properties of  $\text{Fe}_3\text{Sn}_2$  lattice. Given the good agreement between theory and experiment, we expect that the PBE functional is also

suitable to the electronic properties of  $\text{Fe}_3\text{Sn}_2$ . Henceforth, the PBE functional is used throughout this work.

To understand the basic magnetic properties of  $\text{Fe}_3\text{Sn}_2$ , magnetic anisotropy energy (MAE) is calculated and plotted in Figure 1d. In the lowest-energy configuration, all the magnetic moments of Fe atoms are along the same direction. With hexagonal symmetry, the MAE of  $\text{Fe}_3\text{Sn}_2$  exhibits uniaxial anisotropy and can be fit to<sup>[40]</sup>

$$\text{MAE} = K_1 \sin^2 \theta + K_2 \sin^4 \theta \quad (1)$$

where  $\theta$  is the angle of the magnetic moment of the cell relative to the z-axis. The resulting magnetocrystalline anisotropy coefficients are  $K_1 = -0.074 \text{ meV atom}^{-1}$  and  $K_2 = 0.037 \text{ meV atom}^{-1}$ . The easy axis lies in the Fe kagome plane, which is in agreement with experiment at a low temperature.<sup>[41]</sup> The maximum MAE is defined as the energy difference of the system with magnetization axis along the easy axis and perpendicular to it. For practical applications at room temperature, it is crucial to find magnetic nanostructures with MAE up to 0.03–0.05 meV.<sup>[42]</sup> For  $\text{Fe}_3\text{Sn}_2$ , the maximum MAE is calculated to be 0.037 meV per Fe atom, which is close to 2D  $\text{Cr}_2\text{Ge}_2\text{Te}_6$ <sup>[43]</sup> (on the order of  $\approx 0.1 \text{ meV per Cr}$ ), and is about an order of magnitude smaller than 2D  $\text{CrI}_3$ <sup>[44]</sup> (on the order of  $\approx 0.6 \text{ meV per Cr}$ ). This indicates that it may be suitable for spintronic applications.

To investigate magnetic modulation on electronic structures, energy bands and the projected density of states (PDOS) are plotted under different directions of lattice magnetic moment. Figure 2a,b shows the bands and PDOS for the lattice magnetic moment along the x-axis. With the SOC, the electron in a certain state does not have a definite spin. The electronic wavefunction is presented as  $\Psi = (\Psi_\uparrow(\mathbf{r}), \Psi_\downarrow(\mathbf{r}))^T$ , and the spin polarization of a state reads

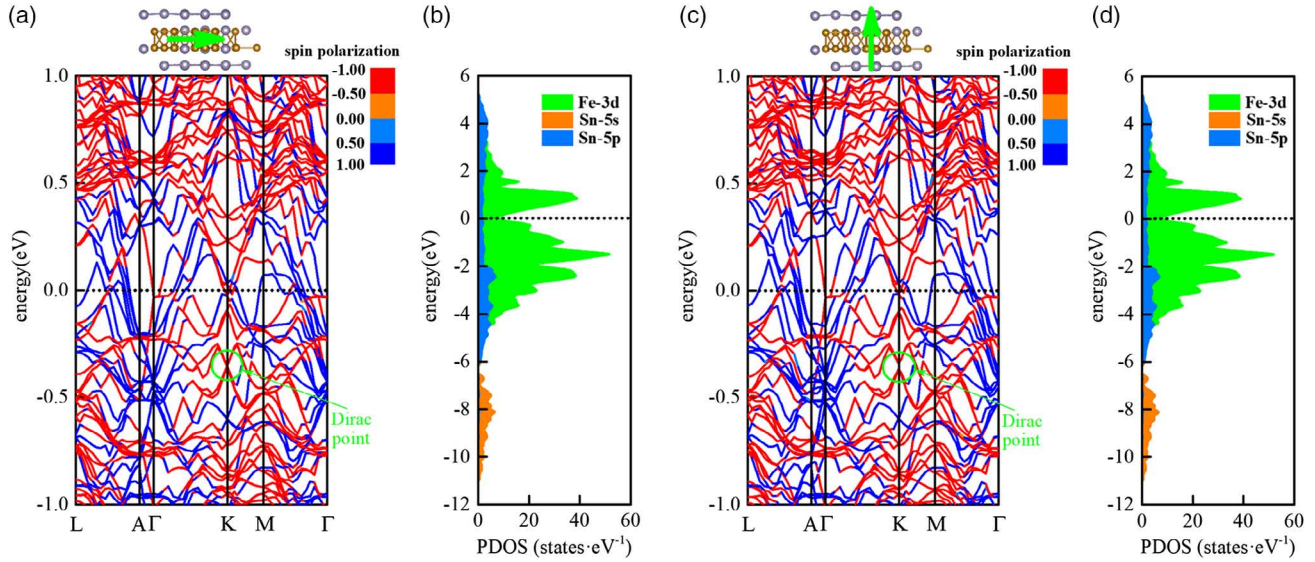


**Figure 2.** Electronic structures of  $\text{Fe}_3\text{Sn}_2$ . a) The band structures and b) PDOS of  $\text{Fe}_3\text{Sn}_2$  lattice with the magnetic moment of the cell along the x-axis. c) The band structures and d) PDOS of  $\text{Fe}_3\text{Sn}_2$  lattice with the magnetic moment of the cell along the z-axis.

$$\int P = \frac{\int \Psi_{\uparrow}(\mathbf{r})d\mathbf{r} - \int \Psi_{\downarrow}(\mathbf{r})d\mathbf{r}}{\int \Psi_{\uparrow}(\mathbf{r})d\mathbf{r} + \int \Psi_{\downarrow}(\mathbf{r})d\mathbf{r}} \quad (2)$$

The polarization of each band state is shown by color in Figure 2a. The energy bands near the Fermi level are mainly composed of Fe 3d orbitals. A Dirac point is found at  $-0.35$  eV below the Fermi level. The electronic states near the Dirac point show a spin-up feature.

When the lattice magnetic moment orients along the z-axis, i.e., perpendicular to Fe kagome planes, the spin-up Dirac point opens a small gap (Figure 2c). The change in the magnetic moment direction does not cause much change in PDOS (Figure 2d). Compared with previous bands shown in Figure 2a, the bands shown in Figure 2c are similar but some gaps in the bands are slightly changed. For comparison, we also show the energy bands at the level of HSE06 (Figure S2a,b, Supporting Information). Because  $\text{Fe}_3\text{Sn}_2$  is a metal, the bands do not show much change under hybrid functional. Such a delicate change can be used to adjust the transport properties of electrons in specific states. In the following subsection, the fundamental principle will be represented.

SOC acts on the Dirac states and influences the electronic properties. In the classical picture, an electron passing through electric field  $\mathbf{E}$  feels an effective magnetic field acting on its spin. For an electron moving at velocity  $\mathbf{V}$ , the magnetic field in the rest frame of the electron reads  $\mathbf{B}_{\text{eff}} = -\frac{1}{c^2}\mathbf{V} \times \mathbf{E}$ . The SOC Hamiltonian reads  $H_{\text{SOC}} = -1/2\boldsymbol{\mu} \cdot \mathbf{B}_{\text{eff}}$ , where  $\boldsymbol{\mu} = -\frac{e}{m}\mathbf{S}$  is the spin magnetic moment of electron and the factor  $1/2$  originates from the Thomas precession. When a 3d electron hops between the second-nearest-neighboring Fe atoms, the chemical environment on both sides of the atomic link line is different. This asymmetry leads to an electric field  $\mathbf{E}$  (Figure S3, Supporting Information) and  $\mathbf{B}_{\text{eff}}$  acting on the electron. For a 3d electron with its spin perpendicular to the Fe kagome plane,  $H_{\text{SOC}}$  would affect the band structure of Dirac electrons and generate an effective mass. For a lattice magnetic moment lying in

the kagome plane,  $H_{\text{SOC}} = 0$  does not affect the Dirac electrons and the effective mass remains zero even when the spin is rotated in the plane.

To reveal the mechanism of the opening gap in the Dirac state, a tight-binding model is used. For the bands with single spin direction, the tight-binding Hamiltonian

$$H_0 = -t \sum_{\langle ij \rangle} c_i^{\dagger} c_j \quad (3)$$

describes the orbital overlapping between the nearest neighboring sites  $i$  and  $j$ , where  $t$  is the interatomic orbital hopping. In momentum space, the Hamiltonian becomes  $H_0 = \sum_{\mathbf{k}} \Psi_{\mathbf{k}}^{\dagger} H_0(\mathbf{k}) \Psi_{\mathbf{k}}$ . In kagome lattice (Figure 3a), the annihilation operator reads  $\Psi_{\mathbf{k}} = (c_{1\mathbf{k}}, c_{2\mathbf{k}}, c_{3\mathbf{k}})^T$ , where  $c_{1\mathbf{k}}$ ,  $c_{2\mathbf{k}}$ , and  $c_{3\mathbf{k}}$  correspond to the Bloch states on atoms 1, 2, and 3. The effective Hamiltonian reads

$$H_0(\mathbf{k}) = -2t \begin{pmatrix} 0 & \cos \mathbf{k} \cdot \mathbf{a}_1 & \cos \mathbf{k} \cdot \mathbf{a}_2 \\ \cos \mathbf{k} \cdot \mathbf{a}_1 & 0 & \cos \mathbf{k} \cdot \mathbf{a}_3 \\ \cos \mathbf{k} \cdot \mathbf{a}_2 & \cos \mathbf{k} \cdot \mathbf{a}_3 & 0 \end{pmatrix} \quad (4)$$

where  $\mathbf{a}_1 = a_0\hat{x}$ ,  $\mathbf{a}_2 = a_0(\hat{x} + \sqrt{3}\hat{y})/2$ , and  $\mathbf{a}_3 = \mathbf{a}_2 - \mathbf{a}_1$  denote the three nearest-neighbor vectors. The energy spectrum of  $H_0(\mathbf{k})$  (dashed lines in Figure 3b) consists of one flat band  $E^{(3)}(\mathbf{k}) = 2t$  and two Dirac bands

$$E^{(1,2)}(\mathbf{k}) = t \left( -1 \pm \sqrt{4(\cos^2 \mathbf{k} \cdot \mathbf{a}_1 + \cos^2 \mathbf{k} \cdot \mathbf{a}_2 + \cos^2 \mathbf{k} \cdot \mathbf{a}_3) - 3} \right) \quad (5)$$

which touch each other at the Dirac points  $\mathbf{K}_{\pm} = \pm 2\pi\hat{x}/3a_0$ . By linearization near  $\mathbf{K}_{\pm}$  and projection onto the subspace associated with bands (1) and (2), the low-energy effective Hamiltonian

$$H_0(\mathbf{k}) = v(\tau_3 k'_x + \tau_1 k'_y) \quad (6)$$

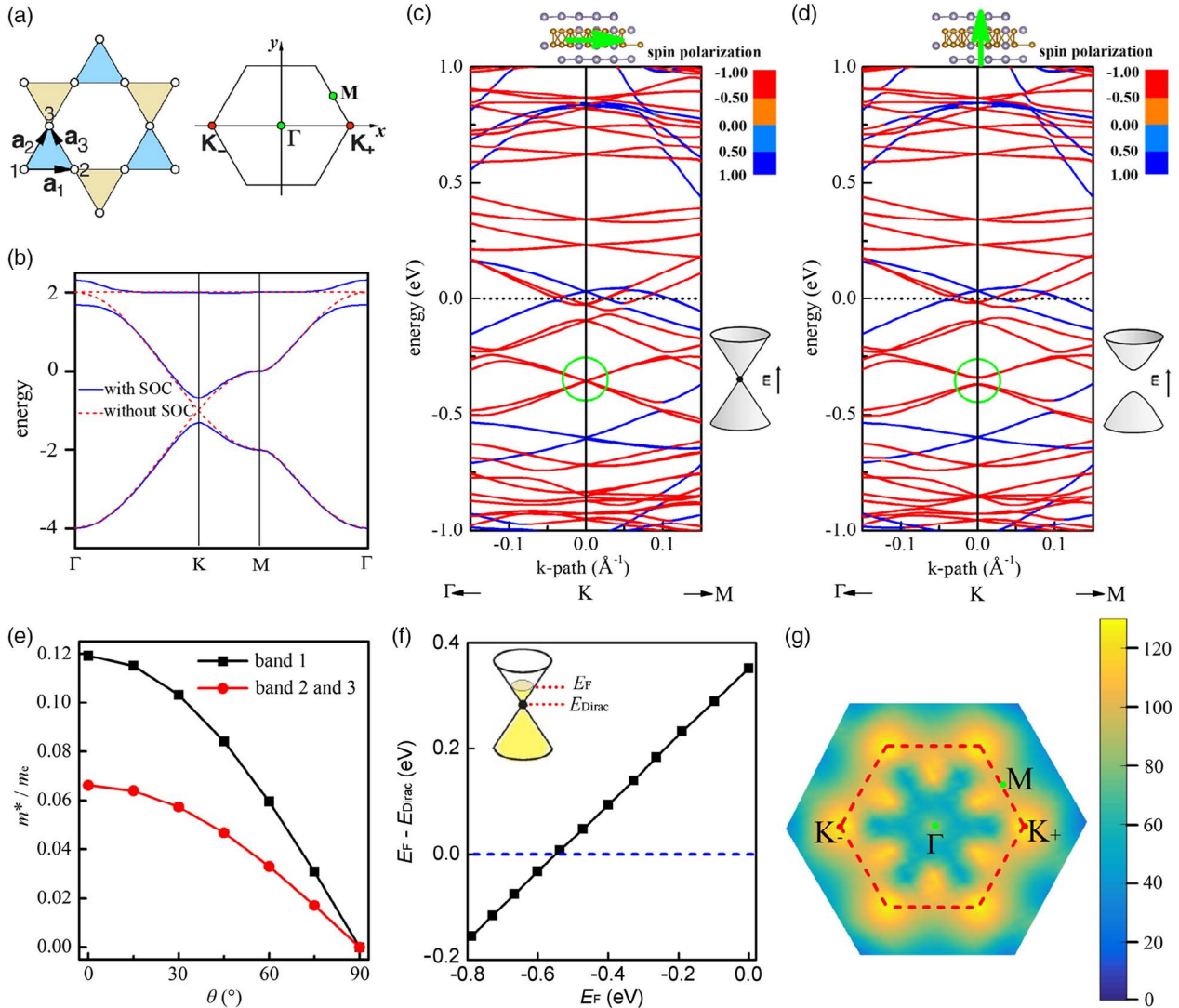


**Figure 3.** Band properties of  $\text{Fe}_3\text{Sn}_2$  near the  $k$ -point. a) The kagome lattice model and the Brillouin zone. b) The energy bands with (blue) and without SOC (red) calculated by the tight-binding model with  $t=1$  and  $\lambda=0.1$ . c) The band structures near the  $k$ -point of  $\text{Fe}_3\text{Sn}_2$  lattice with the magnetic moment of the cell along the  $x$ -axis. d) The band structures near the  $k$ -point of  $\text{Fe}_3\text{Sn}_2$  lattice with the magnetic moment of the cell along the  $z$ -axis. e) The effective mass  $m^*$  of Dirac electrons in bands 1, 2, and 3.  $m_e$  denotes the real electron mass. f) The energy difference  $E_F - E_{\text{Dirac}}$  between the Fermi level and the Dirac mass points varies with the Fermi level  $E_F$ . g) DOS at  $E = E_{\text{Dirac}}$  (in states  $\text{eV}^{-1}$ ).

behaves as Dirac fermion with zero mass. Here, the energy at the Dirac points is set to zero and  $\mathbf{k}' = \mathbf{k} - \mathbf{K}_{\pm}$  is the wave vector near  $\mathbf{K}_{\pm}$ .  $v = \sqrt{3}ta_0$  is Fermi velocity.  $\tau_i$  are Pauli matrices of the pseudospin spanned by the degenerate eigenstates at  $\mathbf{K}_{\pm}$ . The effective Hamiltonian leads to linearly dispersing energy  $E(\mathbf{k}) = \pm vk$ .

SOC leads to the formation of a gap at the Dirac points with the breaking of  $\text{SU}(2)$  spin symmetry. The SOC-induced hopping between the second-nearest neighbors takes the Kane–Mele form<sup>[45,46]</sup>

$$H_{\text{SOC}} = i \frac{2\lambda}{\sqrt{3}a_0^2} \sum_{\langle\langle ij \rangle\rangle} (\mathbf{d}_{1ij} \times \mathbf{d}_{2ij}) \cdot \boldsymbol{\sigma}_{\alpha\beta} c_{i\alpha}^{\dagger} c_{j\beta} \quad (7)$$

where  $\lambda$  is the SOC strength,  $\mathbf{d}_{1ij}$  and  $\mathbf{d}_{2ij}$  are the nearest-neighbor vectors traversed between the second-nearest

neighbors  $i$  and  $j$ , and  $\boldsymbol{\sigma}$  is the Pauli matrices of electronic spin. In kagome lattice, it becomes

$$H_{\text{SOC}} = i\lambda \sum_{\langle\langle ij \rangle\rangle} v_{ij} (c_{i\uparrow}^{\dagger} c_{j\uparrow} - c_{i\downarrow}^{\dagger} c_{j\downarrow}) \quad (8)$$

where  $v_{ij} = -v_{ji} = \pm 1$  depends on the orientation of  $\mathbf{d}_{1ij}$  and  $\mathbf{d}_{2ij}$ .  $v_{ij} = +1$  ( $-1$ ) if the second-nearest hopping is along the anticlockwise (clockwise) direction in the kagome plane.<sup>[45,47]</sup> For a lattice with magnetic moment  $\boldsymbol{\mu}$ , rewrite Equation (8) as

$$H_{\text{SOC}} = i\lambda \sum_{\langle\langle ij \rangle\rangle} v_{ij} (\cos \theta (c_{i\uparrow}^{\dagger} c_{j\uparrow} - c_{i\downarrow}^{\dagger} c_{j\downarrow}) + \sin \theta (c_{i\uparrow}^{\dagger} c_{j\downarrow} + c_{i\downarrow}^{\dagger} c_{j\uparrow})) \quad (9)$$

where  $\theta$  is angle of  $\boldsymbol{\mu}$  relative to the z-axis,  $c_{\boldsymbol{\mu}\uparrow}$  ( $c_{\boldsymbol{\mu}\downarrow}$ ) corresponds to the spin-up (spin-down) state along the direction of  $\boldsymbol{\mu}$ . For Dirac bands with a single spin direction along the direction of  $\boldsymbol{\mu}$ , one expands the SOC Hamiltonian into  $H_{\text{SOC}} = \sum_{\mathbf{k}} \Psi_{\mathbf{k}}^{\dagger} H_{\text{SOC}}(\mathbf{k}) \Psi_{\mathbf{k}}$  in  $\mathbf{k}$  space and obtains

$$H_{\text{SOC}}(\mathbf{k}) = 2i\lambda \cos\theta \begin{pmatrix} 0 & \cos\mathbf{k} \cdot (\mathbf{a}_2 + \mathbf{a}_3) & -\cos\mathbf{k} \cdot (\mathbf{a}_3 - \mathbf{a}_1) \\ \cos\mathbf{k} \cdot (\mathbf{a}_2 + \mathbf{a}_3) & 0 & \cos\mathbf{k} \cdot (\mathbf{a}_1 + \mathbf{a}_2) \\ -\cos\mathbf{k} \cdot (\mathbf{a}_3 - \mathbf{a}_1) & \cos\mathbf{k} \cdot (\mathbf{a}_1 + \mathbf{a}_2) & 0 \end{pmatrix} \quad (10)$$

By projection onto the subspace associated with bands (1) and (2) near  $\mathbf{K}_{\pm}$ , the low-energy effective SOC Hamiltonian reads

$$H_{\text{SOC}}(\mathbf{k}) = \sqrt{3}\lambda \cos\theta (2 - 3k^2 a_0^2/2) \tau_2 \quad (11)$$

The first term leads to the separation of two Dirac bands. The second momentum-quadratic term leads to topological edge states.<sup>[48]</sup> If only considering the first term, the total Hamiltonian

$$H(\mathbf{k}) = H_0(\mathbf{k}) + H_{\text{SOC}}(\mathbf{k}) = v(\tau_3 k'_x + \tau_1 k'_y) + 2\sqrt{3}\lambda \cos\theta \tau_2 \quad (12)$$

behaves as a massive Dirac fermion with an effective rest mass  $m^* = 2\lambda \cos\theta / \sqrt{3}v^2 a_0^2$  that depends on magnetization direction  $\theta$ . It leads to a relativistic momentum–energy relation  $E(\mathbf{k})^2 = m^{*2}v^4 + v^2k'^2$  and a  $\theta$ -dependent bandgap  $\Delta = 4\sqrt{3}\lambda \cos\theta$  between the two Dirac bands.

For  $\theta = 0$ , the energy spectrum of  $H(\mathbf{k})$  is plotted by solid lines in Figure 3b. To verify the prediction of tight-binding model, energy bands near  $\mathbf{K}_{\pm}$  are plotted in detail along the  $\Gamma \rightarrow \mathbf{K}$  and  $\mathbf{K} \rightarrow \mathbf{M}$  paths by DFT calculations. When the lattice magnetic moment  $\boldsymbol{\mu}$  is parallel to the kagome planes (Figure 3c), the up and down Dirac bands meet each other at the Dirac points. In Figure 3c, three Dirac bands that share the same Dirac point in same energy are found (denoted by the green circle). To show more details, atomic orbital–resolved bands are shown in Figure S4, Supporting Information. This triple Dirac point is mainly composed of Fe  $3d_{xy}$  and  $3d_{x^2-y^2}$  orbitals. There also exist other crossing bands at  $\mathbf{K}$ , which are not composed of Fe  $3d_{xy}$  and  $3d_{x^2-y^2}$  orbitals, and thus the above mass mechanism cannot be applied. When the lattice magnetic moment  $\boldsymbol{\mu}$  is perpendicular to the kagome planes (Figure 3d), the three Dirac bands are separated, in which bands 2 and 3 are degenerated. For any lattice magnetic moment  $\boldsymbol{\mu}$  with an orientation  $\theta$ , the effective mass  $m^*$  of the electron can be obtained by fitting the  $k' \approx E(\mathbf{k})$  relation by  $E(\mathbf{k})^2 = m^{*2}v^4 + v^2k'^2$ . Figure 3e shows  $m^*$  with  $\theta$ , showing the previous predicted relation  $m^* = m^*(0) \cdot \cos\theta$ . The earlier results indicate a possible way to modulate electron mass in kagome lattice via controlling the direction of lattice magnetic moment. To exhibit the properties of Dirac states, one can utilize an appropriate positive gate voltage to lower Fermi level to the Dirac points, such as the experiment of anomalous Hall effect in a previous study.<sup>[26]</sup> Because the electrons in the layered kagome lattice behave as  $(2 + 1)$  Dirac fermion, such mass control may benefit research on the simulation of physical effects of high-energy relativistic fermions. By controlling the gate voltage, the Dirac points emerge from below the Fermi level. Figure 3f shows  $E_{\text{F}} - E_{\text{Dirac}}$ , i.e., the energy difference between the Fermi

level and the Dirac points, varying linearly with  $E_{\text{F}}$ . At  $E_{\text{F}} = -0.55$  eV, the Dirac points just emerge at the Fermi level. At this status, the conduction electrons along  $\mathbf{K}_{\pm}$  wave vectors behave as Dirac fermions and the manipulation of mass can be realized. The massive Dirac fermions may be detected on the (0001) kagome surface. Figure 3g shows  $\mathbf{k}$ -resolved density of surface states (DOS) at  $E = E_{\text{Dirac}}$ . The maximum at the  $\mathbf{K}_{\pm}$  points indicates the appearance of Dirac fermions on the surface. Although the Dirac states are submerged in other metallic states, the maximum surface DOS at  $\mathbf{K}_{\pm}$  reveals that the Dirac states govern the surface transport. This may decide the transport properties along the  $\mathbf{K}_{\pm}$  directions.

In this work, we uncover the origin of effective mass of relativistic  $(2+1)$ -dimensional Dirac fermions in  $\text{Fe}_3\text{Sn}_2$  kagome lattice. Theoretical analysis reveals the specificity of spin-polarized Dirac states in  $\text{Fe}_3\text{Sn}_2$ . The Dirac electrons with a unitary spin direction break time-reversal symmetry and provide a possibility to couple with magnetic field. SOC opens a gap between the two Dirac bands with  $\text{SU}(2)$  spin symmetry breaking and gives mass to the Dirac fermions. This effect leads to a relativistic momentum–energy relation and a massive  $(2+1)$  Dirac equation. The effective mass of Dirac electrons is proportional to the SOC strength and relative to the direction of lattice magnetic moment. On this basis, magnetic control to the mass and mobility of Dirac electrons can be implemented. Under a proper gate voltage, the Dirac points in  $\text{Fe}_3\text{Sn}_2$  emerge on the Fermi surface, in which the conduction Dirac electrons can then be manipulated. Our study provides insight into a modulation mechanism based on SOC and guidance for future applications of Dirac materials.

## Computational Section

Electronic structure calculations were carried out within DFT using the projector augmented wave (PAW) method,<sup>[27,28]</sup> as implemented in the Vienna ab initio simulation package.<sup>[29–32]</sup> The PAW potential described the  $[\text{Ne}]3s^2$  states of Fe and the  $[\text{Kr}]4d^{10}$  of Sn as core states. All the calculations used the kinetic energy cutoff of 500 eV. The exchange and correlation of electrons were described using the PBE functional<sup>[33]</sup> at the level of generalized gradient approximation. To verify the reliability, we also carried out comparison calculations using the local density approximation (LDA)<sup>[34]</sup> with/without an effective Hubbard  $U$  parameter.<sup>[35]</sup> The band structures were also calculated using the Heyd–Scuseria–Ernzerhof (HSE06) hybrid functional.<sup>[36,37]</sup> The Brillouin-zone integration was conducted using an  $18 \times 18 \times 5$   $\Gamma$ -centered Monkhorst-Pack grid. The SOC was included in the computation with a full  $k$ -point grid. The convergence of total energy was achieved until the total energy difference of two iterated steps was less than  $10^{-7}$  eV. The atomic positions were fully relaxed until the Hellmann–Feynman forces were below  $0.001$  eV  $\text{\AA}^{-1}$ . The chosen energy cutoff and  $k$ -point meshes ensured the accuracy of the total energy, MAE, and magnetic moments to be  $0.001$  eV  $\text{atom}^{-1}$ ,  $0.001$  meV  $\text{atom}^{-1}$ , and  $0.01$   $\mu_{\text{B}}$   $\text{atom}^{-1}$ , respectively.

## Supporting Information

Supporting Information is available from the Wiley Online Library or from the author.

## Acknowledgements

This work was supported by the Natural Science Basic Research plan in Shaanxi Province of China (grant no. 2018JQ1034).

## Conflict of Interest

The authors declare no conflict of interest.

## Keywords

kagome lattices, massive Dirac fermions, spin-orbit coupling

Received: December 13, 2019

Revised: February 2, 2020

Published online:

- 
- [1] M. Z. Hasan, C. L. Kane, *Rev. Mod. Phys.* **2010**, *82*, 3045.  
 [2] X.-L. Qi, S.-C. Zhang, *Rev. Mod. Phys.* **2011**, *83*, 1057.  
 [3] L. Fu, *Phys. Rev. Lett.* **2011**, *106*, 106802.  
 [4] Z. K. Liu, B. Zhou, Y. Zhang, Z. J. Wang, H. M. Weng, D. Prabhakaran, S. K. Mo, Z. X. Shen, Z. Fang, X. Dai, Z. Hussain, Y. L. Chen, *Science* **2014**, *343*, 864.  
 [5] Z. Wang, Y. Sun, X.-Q. Chen, C. Franchini, G. Xu, H. Weng, X. Dai, Z. Fang, *Phys. Rev. B* **2012**, *85*, 195320.  
 [6] S.-M. Huang, S.-Y. Xu, I. Belopolski, C.-C. Lee, G. Chang, B. Wang, N. Alidoust, G. Bian, M. Neupane, C. Zhang, S. Jia, A. Bansil, H. Lin, M. Zahid Hasan, *Nat. Commun.* **2015**, *6*, 7373.  
 [7] X. Wan, A. M. Turner, A. Vishwanath, S. Y. Savrasov, *Phys. Rev. B* **2011**, *83*, 205101.  
 [8] H. Weng, C. Fang, Z. Fang, B. A. Bernevig, X. Dai, *Phys. Rev. X* **2015**, *5*, 011029.  
 [9] A. A. Burkov, M. D. Hook, L. Balents, *Phys. Rev. B* **2011**, *84*, 235126.  
 [10] C. Fang, H. Weng, X. Dai, Z. Fang, *Chin. Phys. B* **2016**, *25*, 117106.  
 [11] R. Li, H. Ma, X. Cheng, S. Wang, D. Li, Z. Zhang, Y. Li, X.-Q. Chen, *Phys. Rev. Lett.* **2016**, *117*, 096401.  
 [12] R. Yu, H. Weng, Z. Fang, X. Dai, X. Hu, *Phys. Rev. Lett.* **2015**, *115*, 036807.  
 [13] T. E. O'Brien, P. Rožek, A. R. Akhmerov, *Phys. Rev. Lett.* **2018**, *120*, 220504.  
 [14] Z. K. Liu, B. Zhou, Y. Zhang, Z. J. Wang, H. M. Weng, D. Prabhakaran, S.-K. Mo, Z. X. Shen, Z. Fang, X. Dai, Z. Hussain, Y. L. Chen, *Science* **2014**, *343*, 864.  
 [15] Z. K. Liu, J. Jiang, B. Zhou, Z. J. Wang, Y. Zhang, H. M. Weng, D. Prabhakaran, S. K. Mo, H. Peng, P. Dudin, T. Kim, M. Hoesch, Z. Fang, X. Dai, Z. X. Shen, D. L. Feng, Z. Hussain, Y. L. Chen, *Nat. Mater.* **2014**, *13*, 677.  
 [16] Y. Zhao, H. Liu, C. Zhang, H. Wang, J. Wang, Z. Lin, Y. Xing, H. Lu, J. Liu, Y. Wang, S. M. Brombosz, Z. Xiao, S. Jia, X. C. Xie, J. Wang, *Phys. Rev. X* **2015**, *5*, 031037.  
 [17] H. Wang, H. Wang, H. Liu, H. Lu, W. Yang, S. Jia, X. J. Liu, X. C. Xie, J. Wei, J. Wang, *Nat. Mater.* **2016**, *15*, 38.  
 [18] H.-J. Noh, J. Jeong, E.-J. Cho, K. Kim, B. I. Min, B.-G. Park, *Phys. Rev. Lett.* **2017**, *119*, 016401.  
 [19] F. Fei, X. Bo, R. Wang, B. Wu, J. Jiang, D. Fu, M. Gao, H. Zheng, Y. Chen, X. Wang, H. Bu, F. Song, X. Wan, B. Wang, G. Wang, *Phys. Rev. B* **2017**, *96*, 041201(R).  
 [20] M. Yan, H. Huang, K. Zhang, E. Wang, W. Yao, K. Deng, G. Wan, H. Zhang, M. Arita, H. Yang, Z. Sun, H. Yao, Y. Wu, S. Fan, W. Duan, S. Zhou, *Nat. Commun.* **2017**, *8*, 257.  
 [21] J. Kuebler, C. Felser, *Europhys. Lett.* **2016**, *114*, 47005.  
 [22] W. Shi, L. Muechler, K. Manna, Y. Zhang, K. Koepnick, R. Car, J. van den Brink, C. Felser, Y. Sun, *Phys. Rev. B* **2018**, *97*, 060406(R).  
 [23] L.-L. Wang, N. H. Jo, B. Kuthanazhi, Y. Wu, R. J. McQueeney, A. Kaminski, P. C. Canfield, *Phys. Rev. B* **2019**, *99*, 245147s.  
 [24] Z. Wang, M. G. Vergniory, S. Kushwaha, M. Hirschberger, E. V. Chulkov, A. Ernst, N. P. Ong, R. J. Cava, B. Andrei Bernevig, *Phys. Rev. Lett.* **2016**, *117*, 236401.  
 [25] J. Zou, Z. He, G. Xu, *NPJ Comput. Mater.* **2019**, *5*, 96.  
 [26] L. Ye, M. Kang, J. Liu, F. von Cube, C. R. Wicker, T. Suzuki, C. Jozwiak, A. Bostwick, E. Rotenberg, D. C. Bell, L. Fu, R. Comin, J. G. Checkelsky, *Nature* **2018**, *555*, 638.  
 [27] G. Kresse, D. Joubert, *Phys. Rev. B* **1999**, *59*, 1758.  
 [28] P. E. Blöchl, *Phys. Rev. B* **1994**, *50*, 17953.  
 [29] G. Kresse, J. Furthmüller, *Phys. Rev. B* **1996**, *54*, 11169.  
 [30] G. Kresse, J. Furthmüller, *Comput. Mater. Sci.* **1996**, *6*, 15.  
 [31] G. Kresse, J. Hafner, *Phys. Rev. B* **1993**, *47*, 558.  
 [32] G. Kresse, J. Hafner, *Phys. Rev. B* **1994**, *49*, 14251.  
 [33] J. P. Perdew, K. Burke, M. Ernzerhof, *Phys. Rev. Lett.* **1996**, *77*, 3865.  
 [34] J. P. Perdew, A. Zunger, *Phys. Rev. B* **1981**, *23*, 5048.  
 [35] S. L. Dudarev, G. A. Botton, S. Y. Savrasov, C. J. Humphreys, A. P. Sutton, *Phys. Rev. B* **1998**, *57*, 1505.  
 [36] J. Heyd, G. E. Scuseria, M. Ernzerhof, *J. Chem. Phys.* **2003**, *118*, 8207.  
 [37] J. Heyd, G. E. Scuseria, M. Ernzerhof, *J. Chem. Phys.* **2006**, *124*, 219906.  
 [38] L. A. Fenner, A. A. Dee, A. S. Wills, *J. Phys.: Condens. Matter* **2009**, *21*, 452202.  
 [39] H. Giefers, M. Nicol, *J. Alloys Compd.* **2006**, *422*, 132.  
 [40] R. C. O'Handley, *Modern Magnetic Materials: Principles and Applications*, 1st ed., Wiley-Interscience, New York **1999**.  
 [41] G. Le Caër, B. Malaman, B. Roques, *J. Phys. F: Metal Phys.* **1978**, *8*, 323.  
 [42] Y. Zhang, G. Zhu, J. Lu, Z. Guo, J. Cao, *RSC Adv.* **2015**, *5*, 87841.  
 [43] Y. Fang, S. Wu, Z.-Z. Zhu, G.-Y. Guo, *Phys. Rev. B* **2018**, *98*, 125416.  
 [44] V. K. Gudelli, G.-Y. Guo, *New J. Phys.* **2019**, *21*, 053012.  
 [45] C. L. Kane, E. J. Mele, *Phys. Rev. Lett.* **2005**, *95*, 226801.  
 [46] C. L. Kane, E. J. Mele, *Phys. Rev. Lett.* **2005**, *95*, 146802.  
 [47] H.-D. Liu, Y.-H. Chen, H.-F. Lin, H.-S. Tao, J.-H. Wu, *Chin. Phys. B* **2014**, *23*, 077101.  
 [48] S.-Q. Shen, *Topological Insulators – Dirac Equation in Condensed Matters*, Springer Series in Solid-State Sciences, Vol. 174 (Eds: M. Cardona, P. Fulde, K. von Klitzing, R. Merlin, H.-J. Queisser), Springer, Heidelberg, New York, Dordrecht, London **2012**.